

Title

Accurate predictions of keyhole depths using machine learning-aided simulations

Authors

Jiahui Zhang¹, Runbo Jiang², Kangming Li¹, Pengyu Chen¹, Xiao Shang¹, Zhiying Liu¹, Jason Hattrick-Simpers¹, Brian J. Simonds³, Qianglong Wei⁴, Hongze Wang⁴, Tao Sun⁵, Anthony D. Rollett⁶, Yu Zou^{1,*}

Affiliations

¹Department of Materials Science and Engineering, University of Toronto, Toronto, ON M5S 3E4, Canada

²Advanced Light Source (ALS) Division, Lawrence Berkeley National Laboratory, Berkeley, CA 94720, USA

³Applied Physics Division, Physical Measurements Laboratory, National Institute of Standards and Technology, Boulder, CO 80305, USA

⁴School of Materials Science & Engineering, Shanghai Jiao Tong University, Shanghai, 200240, China

⁵Department of Mechanical Engineering, Northwestern University, Evanston, IL 60208, USA

⁶Department of Materials Science and Engineering, Carnegie Mellon University, Pittsburgh, PA 15213, USA

*Corresponding author. Email: mse.zou@utoronto.ca (Y. Z.)

Abstract

The keyhole phenomenon is widely observed in laser materials processing, including laser welding, remelting, cladding, drilling, and additive manufacturing. Keyhole-induced defects, primarily pores, dramatically affect the performance of final products, impeding the broad use of these laser-based technologies. The formation of these pores is typically associated with the dynamic behavior of the keyhole. So far, the accurate characterization and prediction of keyhole features, particularly keyhole depth, as a function of time has been a challenging task. *In situ* characterization of keyhole dynamic behavior using a synchrotron X-ray is complicated and expensive. Current simulations are hindered by their poor accuracies in predicting keyhole depths due to the lack of real-time laser absorptance data. Here, we develop a machine learning-aided simulation method that allows us to accurately predict keyhole depth over a wide range of processing parameters. Based on titanium and aluminum alloys, two commonly used engineering materials as examples, we achieve an accuracy with an error margin of 10 %, surpassing those simulated using other existing models (with an error margin in a range of 50-200 %). Our machine learning-aided simulation method is affordable and readily deployable for a large variety of materials, opening new doors to eliminate or reduce defects for a wide range of laser materials processing techniques.

Introduction

For over half a century, laser materials processing has been broadly used in our society, including aerospace, automotive, energy, medical, and many other high-tech industries^{1,2}. Defects such as pores formed during laser-material interaction, however, pose a serious threat to the mechanical durability, reliability, and security of these components. For example, the fatigue resistance of a component is significantly decreased due to these defects^{3,4}. Keyhole – a deep and narrow cavity caused by the recoil pressure generated by rapid evaporation – plays a pivotal role in generating defects during the laser materials processing processes⁵. The fluctuation and collapse of keyholes typically form bubbles in melts and eventually pores in final products^{6,7}. Yet, the characterization and prediction of keyhole dynamics during laser-material interaction remains a technical challenge because it is a highly localized and ultra-fast process. Recent advancements in high-speed synchrotron X-ray imaging experiments^{8,9} provided insights into keyhole instability under various processing parameters of powers (P) and scan speeds (v)^{10,11}. However, their widespread adoption has been largely impeded by sophisticated instruments and limited access to synchrotron facilities. Hence, there is a compelling need for a low-cost and readily deployable solution to quantify keyhole features for a large variety of processing parameters and materials.

Numerical simulation provides a cost-effective and efficient opportunity to reveal the complex physical mechanisms during laser-metal interaction including recoil pressure, Marangoni convection, material spattering, and porosity generation^{12,13,14}. However, such simulations often fail to accurately predict keyhole dimensions^{15,16}, which is mainly due to the lack of data on real-time laser absorptance. The laser absorptance quantifies the portion of applied laser energy absorbed by the material and is an essential input parameter in simulation models^{17,18,19}. In reported simulation studies, constant laser absorptance is commonly used for a large range of P - v space, for example, 0.3 for Ti-6Al-4V (Ti64) and 0.7 for aluminum (Al)^{20,21}. However, it is not rational to use the same empirical laser absorptance for a large variety of processing parameters because keyhole morphologies are distinct under different parameters, thereby changing real-time laser absorptance²². Although efforts have been made to employ laser multi-reflection simulations to estimate the laser absorptance for different processing parameters^{23,24}, the simulated values and experimental results show obvious disparities due to inherent assumptions in these models²⁵. Furthermore, such simulations typically validate the accuracies of their models within a narrow processing window, rather than a wide one, limiting the simulation methods to be effectively generalized²⁶.

Recently, machine learning has shown exceptional capability to handle multi-dimensional data and discover implicit relationships within a dataset^{27,28,29}. Therefore, new machine learning methods have been widely used in monitoring and measuring keyhole features for laser materials processing^{30,31,32}. Nevertheless, the establishment of an accurate prediction model for dynamic keyhole features is still hindered by the absence of a comprehensive dataset such as laser absorptance values across various processing parameters. In this study, we combine an adopted computational fluid dynamics (CFD) model and a machine learning-based laser absorptance model to visualize real-time keyhole morphologies. Using experimental laser absorptance data, we validate the accuracy of our CFD model and use the CFD model to generate a large laser absorptance dataset based on readily available experimental X-ray images. Employing the generated dataset and machine learning-based method, we accurately predict laser absorptance for subsequent keyhole depth simulation in a large P - v - r_0 space (r_0 is the laser spot radius on the sample surface).

Results

Multi-physics simulations based on real-time laser absorptance measurements

The experimentally measured laser absorptance initially increases and gradually stabilizes, for example, after 0.4 ms for Ti64 and 0.6 ms for Al6061, respectively (Fig 1a and b). The initial high absorption is a start-of-line feature due to keyhole initiation under sufficiently high laser irradiation^{22, 33}. Within the keyhole cavity, the laser undergoes multiple reflections, leading to an increase in the laser absorptance compared to that on a flat surface¹⁸. Meanwhile, a pronounced Marangoni effect³⁴ transports hotter molten metal toward colder regions, resulting in a reduction of the keyhole depth and multiple reflections, which lowers the laser absorptance. Under these conditions, the combined effects of metal vaporization and fluid dynamics maintain the equilibrium of keyhole morphologies, as elucidated in²². In this work, we focus on the period of stable melting, as indicated by the regions between dash lines (Fig 1a and b).

To predict the keyhole depths, we adopted a multi-physics thermal-fluid flow model, using CFD with a volume of fraction (VOF) approach. We compared the time-resolved keyhole depth obtained from simulations and experimental results derived from X-ray images. Our simulation results of keyhole morphologies are comparable to those observed in experimental X-ray images (Fig 1e-h): the simulated keyhole depths (Ti64: $54 \pm 4 \mu\text{m}$; Al6061: $143 \pm 21 \mu\text{m}$) versus experimental keyhole depth (Ti64: $55 \pm 5 \mu\text{m}$; Al6061: $148 \pm 29 \mu\text{m}$). Compared to Ti64, Al typically necessitates a higher energy density input for processing, primarily because of its larger laser reflectivity and the presence of supercritical oxide³⁵. This increased energy density input facilitates the formation of a higher aspect ratio keyhole, boosting the fluctuation frequency of the keyhole¹⁰. Moreover, for all five data points, our simulation results match the experimental results well (Supplementary Fig. 1), demonstrating the consistently high performance of our model.

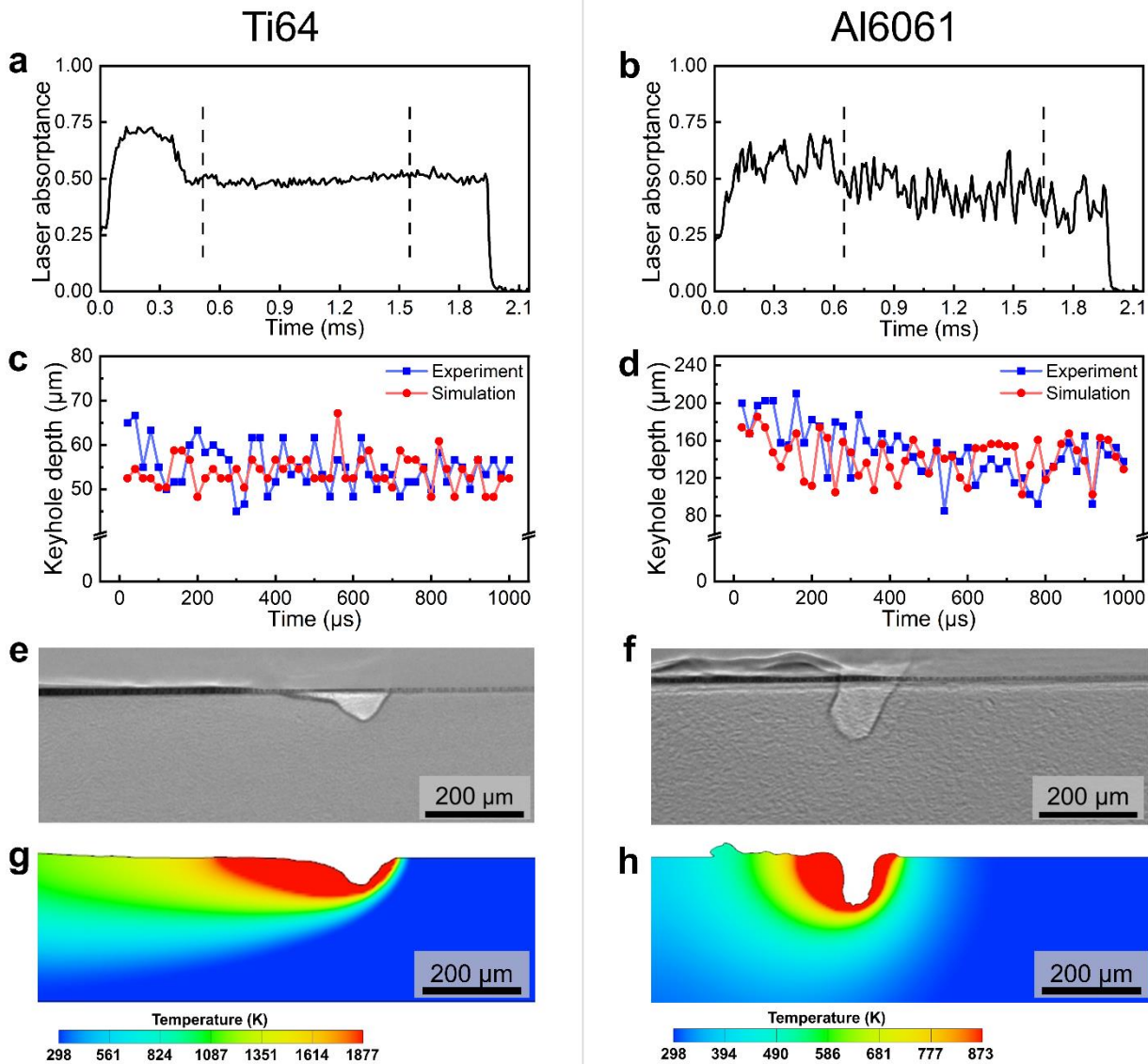


Fig. 1. Multi-physics simulations for Ti64 under a laser power of 200 W and Al6061 under a laser power of 500 W, using the experimental laser absorbance. a, b Experimentally measured real-time laser absorbance. The steady states conditions used for the analysis of keyhole depths are indicated by dashed lines. **c, d** Comparison of keyhole depths generated by our simulation and measured by experiments. This comparison is conducted with a time interval of 1 ms after keyhole fluctuation had reached a plateau. **e, f** Two selected X-ray images showing the keyhole morphologies for Ti64 and Al6061, respectively. **g, h** Simulation results showing temperature contours to compare to **e** and **f**, respectively. The simulated keyhole morphologies match the experimental observations well.

Laser absorbance derivation and dataset generation

Accurate keyhole depth prediction by our simulation model requires real-time laser absorbance, which is not always experimentally available. Consequently, establishing a predictive model for laser absorbance becomes vital, which first necessitates a dataset with laser absorbance values across various process parameters. In this study, we derive additional laser absorbances from the X-ray images acquired from 23 P - v - r_0 combinations for Ti64 and 18 P - v - r_0 combinations for Al6061 in the literature^{6, 10} (Supplementary Fig. 2). We leverage the validated model to derive the laser absorbance value that results in a simulated keyhole depth that agrees with the experimentally

measured value. This process leads to a compiled dataset of laser absorptance for a set of 46 processing parameters, including both experimental and derived values (Supplementary Data 1).

Visual representations of three selected data points under different input energy densities exhibit good agreements in keyhole morphologies between the simulated and experimental results for both Ti64 (Fig. 2a-c) and Al6061 (Fig. 2d-f). The simulation model not only accurately predicts keyhole depth, but also effectively captures other keyhole features that were not used to derive the absorptance values. Moreover, a comparison between the simulated Al6061 melt pool depth and experimental values analyzed from the X-ray images (Supplementary Fig. 3) validates the accuracy of the derived laser absorptance. Our results indicate the feasibility of accurately deriving laser absorptance from X-ray images of the keyhole.

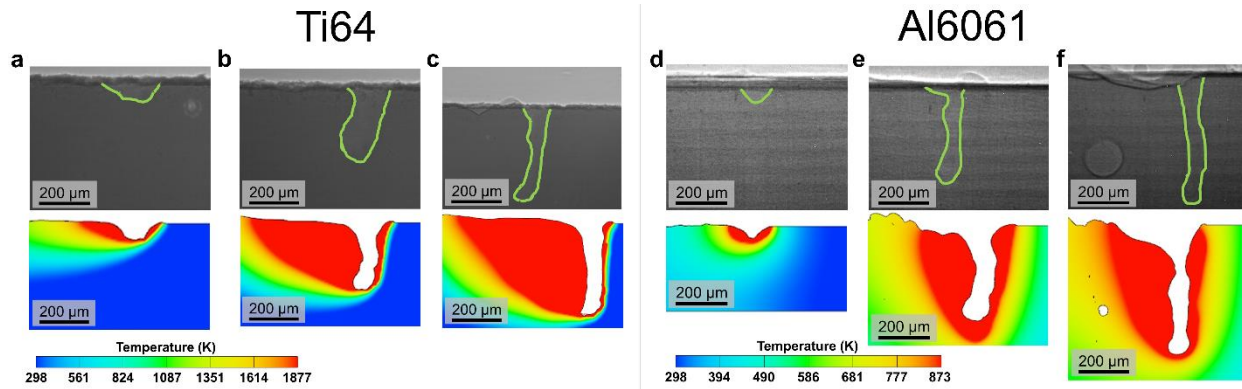


Fig. 2. Visualization of the comparison between simulated and experimental results under various input energy densities. Case studies of Ti64 conducted under following processing parameters: **a** P : 140 W, v : 0.9 m/s, and r_0 : 50 μm ; **b** P : 368 W, v : 0.8 m/s, and r_0 : 50 μm ; **c** P : 540 W, v : 0.8 m/s, and r_0 : 50 μm . Case studies of Al6061 conducted under following processing parameters: **d** P : 140 W, v : 0.9 m/s, and r_0 : 50 μm ; **e** P : 368 W, v : 0.8 m/s, and r_0 : 50 μm ; **f** P : 540 W, v : 0.8 m/s, and r_0 : 50 μm . Despite the significant variations in keyhole morphologies due to the changes of input energy densities, our simulation results match the experimental observations well.

A physics-based approach for keyhole depths prediction

Based on the generated dataset, we employ two approaches to predict the laser absorptance under new processing parameters for Ti64 and Al6061: a physics-based approach and a machine learning-based approach. The physics-based approach resolves the laser absorptance and keyhole depth using physical models that integrate a forward simulation model (*SIM*) with a backward analytical model (*ANA*). The forward simulation model is used to predict the keyhole depth given the laser absorptance (*LA*) and the processing parameters (P , v , and r_0), while the backward analytical model is designed to forecast the laser absorptance value based on the keyhole depth (*KD*) and the processing parameters. The iterative solutions of laser absorptance and keyhole depth are calculated using the following equations:

$$\text{Equations: } \begin{cases} KD = SIM(P, v, r_0, LA) \\ LA = ANA(KD, P, v, r_0) \end{cases} \quad (1)$$

$$\text{Solve: } ANA \left(P, v, r_0, SIM(LA, P, v, r_0) \right) = LA \quad (2)$$

The backward analytical model is approximated using a linear regression function between laser absorptance and a dimensionless variable X , drawing on Gan's work³⁶.

$$X = \frac{KD \cdot (T_l - T_0) \cdot \pi \cdot \rho \cdot C_p \cdot \sqrt{\alpha \cdot v \cdot r_0}}{P} \quad (3)$$

which are calculated using liquidus temperature T_l (K), substrate temperature T_0 (K), density ρ (g/cm³), heat capacity C_p (J/K), thermal diffusivity α (m²·s⁻¹), and keyhole depth KD (m). This backward analytical model is trained using the generated dataset. In laser materials processing, the r_0 also plays a vital role in the melting and evaporation of the material³⁷. This motivated the adaptation of the backward analytical models (between laser absorptance and X) under different r_0 (Fig. 3a and b).

Fig. 3c shows that the iterative process converged during the fifth iteration when using the physics-based approach (P : 196 W, v : 1 m/s, and r_0 : 50 μ m for Ti64) and we observed a 36 % discrepancy between the simulated and experimental keyhole depths ($95 \pm 6 \mu$ m vs. $72 \pm 3 \mu$ m). Such discrepancy is mainly due to the moderately linear correlation between laser absorptance and X , as indicated by a Pearson coefficient of 0.87 (Fig. 3a). This moderate linear relationship indicates that a significant degree of error persists during the iterations of the laser absorptance prediction. For Al6061, the convergence sensitivity under new processing parameters (P : 540 W, v : 0.6 m/s, and r_0 : 50 μ m) requires adjustments to the initial laser absorptance value. Although the initial laser absorptance value is adjusted from 1 to 0.5 for the subsequent iterations to facilitate the process, the backward analytical model still fails to converge (Fig. 3d). Although lowering the initial laser absorptance facilitates iteration convergence in this specific case, the result may not be extrapolatable for various processing parameters. Our results suggest that the physics-based approach is theoretically applicable, but the practical challenges posed by the linear approximation and divergence issue hinder its accurate prediction of keyhole depths.

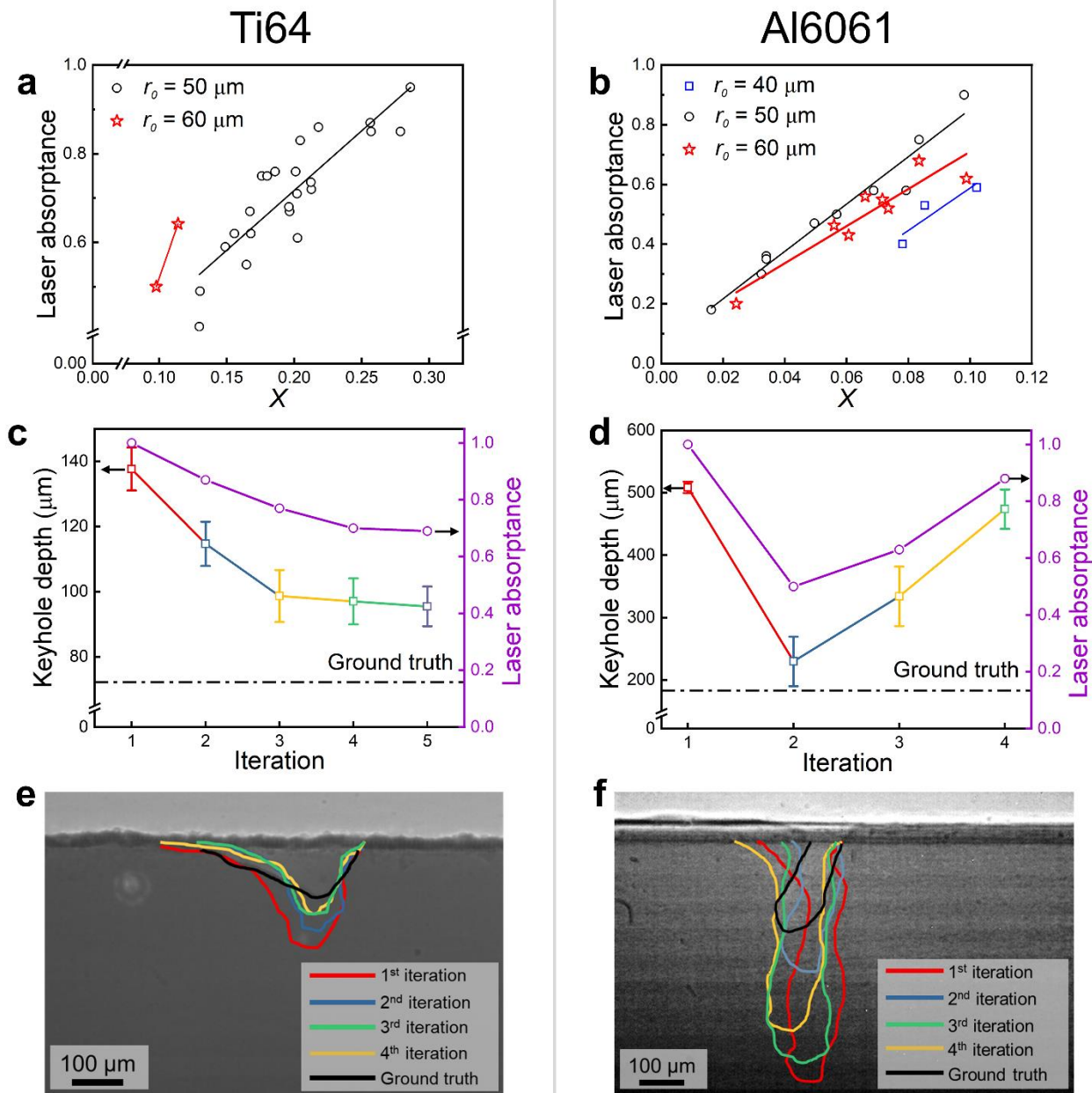


Fig. 3. A physics-based approach designed to predict the laser absorptance and keyhole depth. Analytical models for **a** Ti64 and **b** Al6061 are constructed using a linear relationship between the laser absorptance and a dimensionless variable X . **c** A case study of Ti64 conducted under selected processing parameters (P : 196 W, v : 1 m/s, and r_0 : 50 μm). **d** A case study of Al6061 conducted under selected processing parameters (P : 540 W, v : 0.6 m/s, and r_0 : 50 μm). **e, f** Simulated keyhole shape for each iteration overlaid on the raw X-ray images with distinct colors. The experimental keyhole shape is outlined with the black line. The results show that the physics-based approach fails to predict the keyhole morphologies accurately, especially for Al6061.

A machine learning-based approach for keyhole depths prediction

We use the machine learning-based approach to predict laser absorptance based on processing parameters. The predicted laser absorptance value is subsequently incorporated into the established simulation model to predict the keyhole dynamic behavior. To select the appropriate machine

learning model, we consider six classic regression models: linear regression (LR), support vector regression (SVR), decision tree (DT), random forest (RF), neural network (NN), and Gaussian process regression (GPR). The performance of all the regression models is evaluated using the mean absolute percentage error (MAPE) metric, according to the following equation:

$$MAPE = \frac{1}{n} \sum_{t=1}^n \left| \frac{Y_{PRE_t} - Y_{EXP_t}}{Y_{EXP_t}} \right| \quad (4)$$

where Y_{PRE_t} and Y_{EXP_t} are the predicted and experimental laser absorptance for the t th sample, respectively. Table 1 shows the performance of all the selected regression models. The GPR model is the top-performing model in predicting laser absorptance, making it our choice for the predictive model. The GPR models for laser absorptance prediction are accessible via this link: <https://github.com/Barry-ZhangUofT/ML-model-for-the-LA/tree/main>.

Subsequently, we incorporate both the laser absorptance predicted by the GPR model and laser absorptance from the literature^{20, 21} into the simulation model to predict the keyhole depths under identical processing parameters as the physics-based approach. Our results show that the machine learning-based approach achieves the highest accuracy in predicting keyhole depths with the shortest time of implementation, compared with the other approaches (Fig. 4). The ground truth of keyhole depth is analyzed from time-resolved experimental X-ray images. The simulated keyhole depths within a time interval of 1 ms from all three approaches (i.e., literature-based, physics-based, and machine learning-based) are illustrated (Fig. 4a and b). Furthermore, we show visual representations of keyhole morphology simulated by these three approaches, paired with X-ray images (Fig. 4 a1-a4 and b1-b4), suggesting machine learning-based approach accurately replicates the ground truth of keyhole morphology. Our videos also show the virtualized comparison between experimental X-ray videos and keyhole fluctuations simulated, indicating that our machine learning-based approach best matches the experimental results (Supplementary Videos 6 and 7).

Table 1. The Mean Absolute Percentage Error (MAPE) values for the six regression models in predicting laser absorptance (LA).

Regression models	MAPE for LA (%)	
	Ti64	Al6061
LR	9.4 ± 4.5	31.8 ± 11
DT	9.6 ± 2.7	31.7 ± 15.7
RF	8.6 ± 1.3	26.5 ± 12.6
ANN	10.4 ± 5.6	25.2 ± 13.7
SVR	9.8 ± 3.5	29.3 ± 15.8
GPR	7.6 ± 4	11.5 ± 4.5

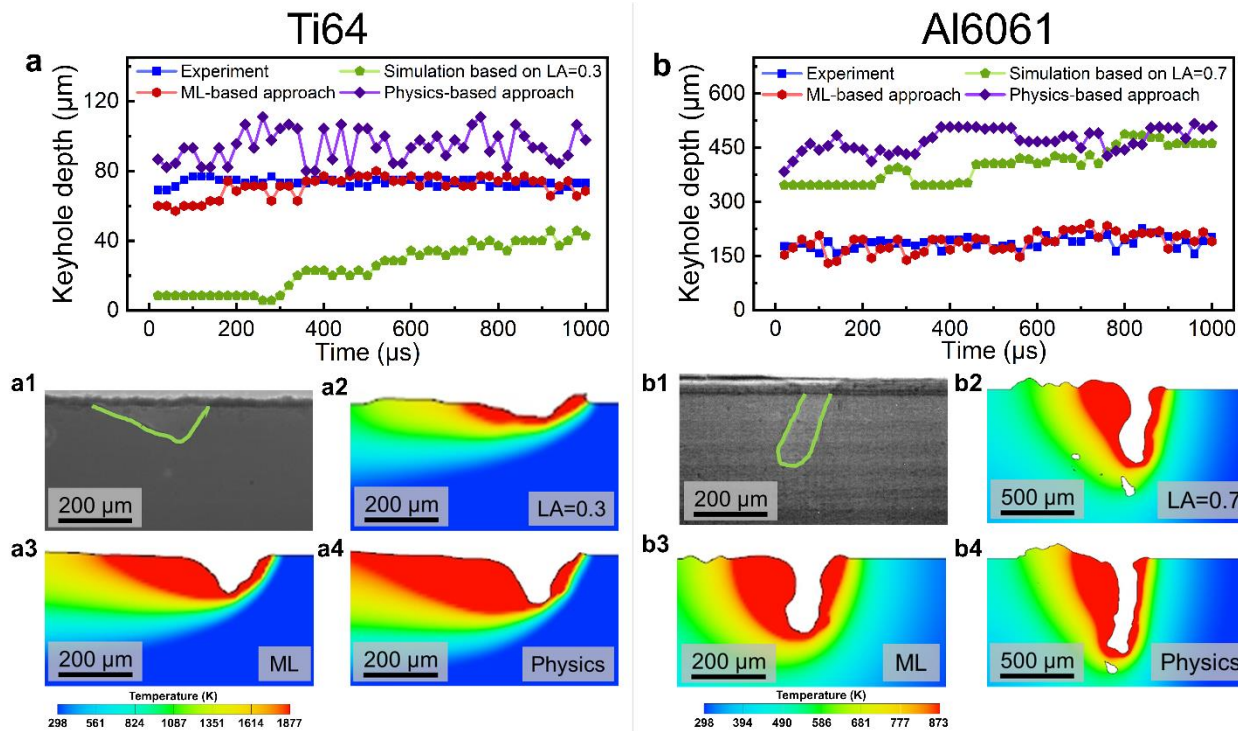


Fig. 4. Comparative analysis of three methods for keyhole instability prediction against experimental results for Ti64 (P : 196 W, v : 1 m/s, and r_0 : 50 μm) and Al6061 (P : 540 W, v : 0.6 m/s, and r_0 : 50 μm). **a, b** Comparison of keyhole depths simulated by three approaches and measured in experiments over a time interval of 1 ms. X-ray images showing keyhole morphologies for **a1** Ti64 and **b1** Al6061. Visualization of keyhole morphologies for **a2-a4** Ti64 and **b2-b4** Al6061, simulated by the method from the literature (fixed laser absorptance (LA) of 0.3 for Ti64 and 0.7 for Al6061), machine learning-based (ML) approach, and physics-based approach, respectively.

Discussion

Overall, by incorporating the CFD model with the experimental laser absorptance, we accurately predict the real-time keyhole depth under various P , v , and r_0 processing conditions for Ti64 and Al6061, maintaining accuracy within a 10 % margin. Leveraging the accuracy of the CFD model, we generate a dataset comprising laser absorptance from 25 P - v - r_0 combinations for Ti64 and 21 P - v - r_0 combinations for Al6061. Subsequently, a GPR model is selected and trained based on this dataset to predict laser absorptance under new processing parameters. Our method, using laser absorptance predicted by the GPR model, leads to improved accuracy and robustness in predicting keyhole depth compared to the approach outlined in the literature^{20, 21}. Our model obviates the need for expensive and labor-intensive experiments under all possible processing conditions and provides a pathway for researchers who do not have access to synchrotrons, offering them an opportunity to enhance their model predictions.

To broaden the applicability of the simulation model, there are several potential improvements. First, although the simulation model is successful in predicting the keyhole depth, incorporating a more accurate laser model may further enhance the simulations of additional keyhole features such as keyhole width and the angle of the keyhole front wall. Second, extending current laser absorptance prediction models to encompass a broader range of materials commonly utilized in laser processing technologies will significantly widen the application scenarios of the model. These

potential improvements will not only enhance the accuracy and versatility of the simulation model but also contribute to advancing our fundamental understanding and control of laser-based techniques across a wide range of materials and processing parameters.

Methods

Data processing and quantification

To enhance the quantification of keyhole morphologies from the raw X-ray images, we employed a segmentation process to isolate the keyhole area and automatically measure its dimensions, following the procedures outlined in ³⁸. For the simulation results, we evaluated the keyhole depth and melt pool depth by referencing the isotherms corresponding to the saturation temperature and solidus temperature of the material, respectively, as suggested by Gan *et al.* ³⁶. To mitigate the influence of volatile fluctuations in keyhole depth calculations, we employed a statistical approach, calculating mean values while excluding the top and bottom 30 % of the data points. We illustrated these processes with an example showcasing the raw X-ray images, segmented mask, and simulation results, including keyhole and melt pool contour lines (Supplementary Fig. 4).

Detailed procedures of the physics-based approach

The detailed steps of the physics-based approach were as follows. The inputs for the loop were exclusively processing parameters: P , v , and r_0 . Initially, the laser absorptance was set to 1. The processing parameters and the laser absorptance value were subsequently fed into the established forward simulation model to compute the keyhole depth. Subsequently, the simulated keyhole depth was passed into the backward analytical model to estimate the laser absorptance that serves as the updated laser absorptance for the next iteration. This iterative process continued until the input laser absorptance of the i^{th} iteration closely converged with the input laser absorptance of the $(i+1)^{th}$ iteration, with a convergence criterion set at 0.01.

Machine learning models

We selected and employed six commonly used machine learning-based regression models to predict laser absorptance under varying processing parameters. We implemented a 5-fold nested cross-validation technique to train these models. For this study, the hyperparameters of all selected models were fine-tuned through a Bayesian optimization algorithm with an acquisition function of expected improvement via a commercially available software regression learner toolbox ³⁹. The first regression model we selected was linear regression (LR) ⁴⁰ due to its simplicity, adaptability, and computational efficiency. To address noise and enhance robustness, we used the support vector regression (SVR) model ⁴¹ and further optimized its kernel function and corresponding scale values. Moreover, the decision tree (DT) ⁴² model was chosen to capture non-linear relationships and we employed random forest (RF) as an ensemble method to mitigate overfitting and instability ⁴³. We hyper-tuned the minimum leaf size and number of learners for the RF model. Artificial neural networks (ANN) ⁴⁴ were included for their ability to analyze intricate nonlinear relationships, optimized by tuning the number of layers and layer size. Lastly, the Gaussian process regression (GPR) model ⁴⁵ was included due to its usability and flexibility in implementation, with optimization of kernel functions and scale values.

Acknowledgments

The authors thank V. Malave, N. Tomlin, and J. Lehman from NIST for their helpful comments on the manuscript. J.Z. acknowledges the valuable suggestions for the preparation of figures and videos from Y. Lyu from the University of Toronto. This research used resources of the Advanced Photon Source; a U.S. Department of Energy (DOE) Office of Science user facility operated for the DOE Office of Science by Argonne National Laboratory under Contract No. DE-AC02-06CH11357. The work is acknowledged of Prof. T. Sun in designing and implementing the apparatus used to obtain the high-speed x-ray images used herein.

Funding: J.Z. and Y.Z. acknowledge the financial support from the Centre for Analytics and Artificial Intelligence Engineering (CARTE) Seed Funding program, Data Sciences Institute Catalyst Grant, and NSERC Alliance Grants—Missions ALLRP 570708-2021. This research is part of the University of Toronto’s Acceleration Consortium, which receives funding from the Canada First Research Excellence Fund (CFREF).

Author contributions:

Conceptualization: J.Z., K.L., J.H.S., and Y.Z.

Methodology: J.Z., Q.W., and H.W.

Investigation: J.Z., R.J., B.J.S., T.S., and A.D.R

Visualization: P.C., Z.L., and X.S.

Funding acquisition: Y.Z.

Project administration: Y.Z.

Supervision: Y.Z.

Writing – original draft: J.Z. and Y.Z.

Writing – review & editing: R.J., K.L., P.C., X.S., Z.L., J.H.S., B.J.S., Q.W., H.W., T.S., and A.D.R.

Competing interests: All authors declare no financial or non-financial competing interests.

Data and materials availability: The time-resolved laser absorptance and the X-ray images acquired at the same time under a laser power of 200 W and a scan speed of 0.7 m/s are available on the NIST Public Data Repository ⁴⁶. Other absorption datasets can be made available upon reasonable request to B.J.S. The X-ray dataset can be made available upon reasonable request to A.D.R. The dataset of segmented keyhole images can be made available upon reasonable request to Y.Z. Additional data including the codes are available from the corresponding authors upon reasonable request.

References

1. Liu Z, He B, Lyu T, Zou Y. A review on additive manufacturing of titanium alloys for aerospace applications: Directed energy deposition and beyond Ti-6Al-4V. *JOM* **73**, 1804-1818 (2021).
2. Steen WM, Mazumder J. *Laser material processing*. Springer science & business media (2010).
3. Leuders S, *et al.* On the mechanical behaviour of titanium alloy TiAl6V4 manufactured by selective laser melting: Fatigue resistance and crack growth performance. *Int J Fatigue* **48**, 300-307 (2013).
4. Zhao X, *et al.* Comparison of the microstructures and mechanical properties of Ti-6Al-4V fabricated by selective laser melting and electron beam melting. *Materials & Design* **95**, 21-31 (2016).
5. Cunningham R, *et al.* Keyhole threshold and morphology in laser melting revealed by ultrahigh-speed x-ray imaging. *Science* **363**, 849-852 (2019).
6. Zhao C, *et al.* Critical instability at moving keyhole tip generates porosity in laser melting. *Science* **370**, 1080-1086 (2020).
7. Hojjatzadeh SMH, *et al.* Pore elimination mechanisms during 3D printing of metals. *Nature communications* **10**, 3088 (2019).
8. Zhao C, *et al.* Real-time monitoring of laser powder bed fusion process using high-speed X-ray imaging and diffraction. *Scientific reports* **7**, 3602 (2017).
9. Leung CLA, *et al.* Laser-matter interactions in additive manufacturing of stainless steel SS316L and 13-93 bioactive glass revealed by in situ X-ray imaging. *Additive Manufacturing* **24**, 647-657 (2018).
10. Huang Y, *et al.* Keyhole fluctuation and pore formation mechanisms during laser powder bed fusion additive manufacturing. *Nature Communications* **13**, 1170 (2022).
11. Leung CLA, Marussi S, Atwood RC, Towrie M, Withers PJ, Lee PD. In situ X-ray imaging of defect and molten pool dynamics in laser additive manufacturing. *Nature communications* **9**, 1355 (2018).
12. Guo L, *et al.* A high-fidelity comprehensive framework for the additive manufacturing printability assessment. *Journal of Manufacturing Processes* **105**, 219-231 (2023).
13. Wang L, Zhang Y, Chia HY, Yan W. Mechanism of keyhole pore formation in metal additive manufacturing. *npj Computational Materials* **8**, 22 (2022).
14. Khairallah SA, Anderson AT, Rubenchik A, King WE. Laser powder-bed fusion additive manufacturing: Physics of complex melt flow and formation mechanisms of pores, spatter, and denudation zones. *Acta Mater* **108**, 36-45 (2016).

15. Moges T, Ameta G, Witherell P. A review of model inaccuracy and parameter uncertainty in laser powder bed fusion models and simulations. *Journal of manufacturing science and engineering* **141**, 040801 (2019).
16. Cook PS, Ritchie DJ. Determining the laser absorptivity of Ti-6Al-4V during laser powder bed fusion by calibrated melt pool simulation. *Optics & Laser Technology* **162**, 109247 (2023).
17. Grange D, Queva A, Guillemot G, Bellet M, Bartout JD, Colin C. Effect of processing parameters during the laser beam melting of Inconel 738: Comparison between simulated and experimental melt pool shape. *J Mater Process Technol* **289**, 116897 (2021).
18. Trapp J, Rubenchik AM, Guss G, Matthews MJ. In situ absorptivity measurements of metallic powders during laser powder-bed fusion additive manufacturing. *Applied Materials Today* **9**, 341-349 (2017).
19. Ye J, *et al.* Energy coupling mechanisms and scaling behavior associated with laser powder bed fusion additive manufacturing. *Adv Eng Mater* **21**, 1900185 (2019).
20. Wang H, Zou Y. Microscale interaction between laser and metal powder in powder-bed additive manufacturing: conduction mode versus keyhole mode. *Int J Heat Mass Transfer* **142**, 118473 (2019).
21. Guo L, *et al.* Understanding keyhole induced-porosities in laser powder bed fusion of aluminum and elimination strategy. *International Journal of Machine Tools and Manufacture* **184**, 103977 (2023).
22. Simonds BJ, *et al.* The causal relationship between melt pool geometry and energy absorption measured in real time during laser-based manufacturing. *Applied Materials Today* **23**, 101049 (2021).
23. Kaiser TB. Laser ray tracing and power deposition on an unstructured three-dimensional grid. *Physical Review E* **61**, 895 (2000).
24. Cho J-H, Na S-J. Implementation of real-time multiple reflection and Fresnel absorption of laser beam in keyhole. *J Phys D: Appl Phys* **39**, 5372 (2006).
25. Ganeriwala RK, Hodge NE, Solberg JM. Towards improved speed and accuracy of laser powder bed fusion simulations via multiscale spatial representations. *Computational Materials Science* **187**, 110112 (2021).
26. Guo L, *et al.* Identifying the keyhole stability and pore formation mechanisms in laser powder bed fusion additive manufacturing. *J Mater Process Technol* **321**, 118153 (2023).
27. Gu D, Shi X, Poprawe R, Bourell DL, Setchi R, Zhu J. Material-structure-performance integrated laser-metal additive manufacturing. *Science* **372**, eabg1487 (2021).
28. DebRoy T, Mukherjee T, Wei HL, Elmer JW, Milewski JO. Metallurgy, mechanistic models and machine learning in metal printing. *Nature Reviews Materials* **6**, 48-68 (2021).

29. Wang C, Tan XP, Tor SB, Lim CS. Machine learning in additive manufacturing: State-of-the-art and perspectives. *Additive Manufacturing* **36**, 101538 (2020).
30. Shevchik S, *et al.* Supervised deep learning for real-time quality monitoring of laser welding with X-ray radiographic guidance. *Scientific reports* **10**, 3389 (2020).
31. Ren Z, *et al.* Machine learning–aided real-time detection of keyhole pore generation in laser powder bed fusion. *Science* **379**, 89-94 (2023).
32. Jiang R, Smith J, Yi Y-T, Sun T, Simonds BJ, Rollett AD. Deep learning approaches for instantaneous laser absorptance prediction in additive manufacturing. *npj Computational Materials* **10**, 6 (2024).
33. Mayi YA, Dal M, Peyre P, Bellet M, Fabbro R. Physical mechanisms of conduction-to-keyhole transition in laser welding and additive manufacturing processes. *Optics & Laser Technology* **158**, 108811 (2023).
34. Mills KC, Keene BJ, Brooks RF, Shirali A. Marangoni effects in welding. *Philosophical Transactions of the Royal Society of London Series A: Mathematical, Physical and Engineering Sciences* **356**, 911-925 (1998).
35. Tang M, Pistorius PC. Fatigue life prediction for AlSi10Mg components produced by selective laser melting. *Int J Fatigue* **125**, 479-490 (2019).
36. Gan Z, *et al.* Universal scaling laws of keyhole stability and porosity in 3D printing of metals. *Nature communications* **12**, 2379 (2021).
37. Sow MC, *et al.* Influence of beam diameter on Laser Powder Bed Fusion (L-PBF) process. *Additive Manufacturing* **36**, 101532 (2020).
38. Zhang J, *et al.* Image Segmentation for Defect Analysis in Laser Powder Bed Fusion: Deep Data Mining of X-Ray Photography from Recent Literature. *Integrating Materials and Manufacturing Innovation* **11**, 418-432 (2022).
39. Snoek J, Larochelle H, Adams RP. Practical bayesian optimization of machine learning algorithms. *Advances in neural information processing systems* **25**, (2012).
40. Montgomery DC, Peck EA, Vining GG. *Introduction to linear regression analysis*. John Wiley & Sons (2021).
41. Smola AJ, Schölkopf B. A tutorial on support vector regression. *Statistics and computing* **14**, 199-222 (2004).
42. Von Winterfeldt D, Edwards WJ. *Decision analysis and behavioral research*. (1986).
43. Ho TK. Random decision forests. In: *Proceedings of 3rd international conference on document analysis and recognition*. IEEE (1995).
44. Jain AK, Mao J, Mohiuddin KM. Artificial neural networks: A tutorial. *Computer* **29**, 31-44 (1996).

45. Williams C, Rasmussen C. Gaussian processes for regression. *Advances in neural information processing systems* **8**, (1995).
46. Simonds BJ, *et al.* Ability to Simulate Absorption and Melt Pool Dynamics for Laser Melting of Bare Aluminum Plate: Results and Insights from the 2022 Asynchronous AM-Bench Challenge. *Integrating Materials and Manufacturing Innovation*, 1-10 (2024).
47. Shrestha S, Kevin Chou YJJoMS, Engineering. A numerical study on the keyhole formation during laser powder bed fusion process. *Journal of Manufacturing Science and Engineering* **141**, 101002 (2019).

Supplementary Materials for
Accurate predictions of keyhole depths using machine learning-aided
simulations

Jiahui Zhang *et al.*

* Corresponding author. Email: mse.zou@utoronto.ca (Y. Z.)

This PDF file includes:

Supplementary Text
Supplementary Figures 1 to 6
Supplementary Tables 1

Other Supplementary Materials for this manuscript include the following:

Supplementary Video 1 to 7
Supplementary Data 1

Supplementary Text

Experimental Investigations on Laser Absorptance and X-ray Image Capture

A combined integrating sphere and high-speed synchrotron X-ray system was developed to measure laser energy absorptance and capture the X-ray videos at the 32-ID-B beamline of Advanced Photon Source at Argonne National Laboratory. The absorbed laser energy is calculated using an energy balance computation between the measured input and scattered laser light (zero light transmission). To ensure the collection of intense backscattered light from the initially specular surface, the laser incident was at an angle of 7° relative to the sample surface normal. A fiber-coupled photodiode positioned on the sphere surface was used to measure the backscattered light. The resulting photodiode voltage was captured by a high-speed oscilloscope, providing a voltage uncertainty of 1 % and a time resolution of 40 ns. To establish an absolute measurement of the scattered light power, a calibration procedure was conducted using a well-characterized scattering surface instead of the experimental target, enabling the conversion of the photodiode signal into an accurate measurement of the scattered light power. More detailed information about the laser absorptance measurements can be found in Ref ²². Experiments were conducted on two P & v combinations for Ti64 and three for Al6061 under a constant surface spot radius of 60 μm on bare plates to acquire the real-time laser absorptance data from the first to last moments of laser exposure.

The laser system utilized in the experiments comprises a ytterbium fiber laser and a galvo laser scanner system. The fiber laser operates at a wavelength of 1070 nm with a maximum power output of 540 W. The laser's maximum traversal speed across the sample is 2 m/s. To maintain controlled conditions, the samples are enclosed within a stainless-steel chamber with an argon (Ar) environment at atmospheric pressure (1 atm). During the experimental setup, the laser interacts with the specimen, while high-energy X-rays penetrate through its thickness. Concurrently, a high-speed camera captures images at a rapid frame rate of 50,000 frames per second. For the X-ray images captured alongside the laser absorptance measurements for both Ti-6Al-4V (Ti64) and Al6061, the laser spot diameter on the sample surface is 122.5 μm , and the laser spot diameter on the focal plane is 49.5 μm . For the X-ray images collected from the literature for Ti64, the laser spot diameter on the sample surface is 95 μm , and the laser spot diameter on the focal plane is 56 μm . The laser spot diameters on the sample surface for Al6061 are 82.5, 95, and 122.5 μm , respectively. To simplify calculations, we approximate the laser spot radii on the sample surface for simulation models as 60, 50, and 40 μm , respectively.

Multiphysics thermal-fluid flow model

In this study, we adopted a multi-physics thermal-fluid flow model, using computational fluid dynamics (CFD) and volume of fraction (VOF) approaches, implemented through Flow 3d v11.2 (Please note that certain commercial products or company names are identified here to describe our study adequately. Such identification is not intended to imply recommendation or endorsement by the National Institute of Standards and Technology, nor is it intended to imply that the products or names identified are necessarily the best available for the purpose).

The numerical simulation is based on a set of model assumptions: (1) the liquid in the melt pool is incompressible and Newtonian; (2) the shielding gas is ignored, and the area other than the fluid is treated as void with uniform temperature and pressure; (3) phase change is considered while the resulting compositional change is omitted; and (4) the vapor is not modeled but the effect is considered through recoil pressure ²¹.

The mass conservation equation, Navier-Stokes equation, and energy conservation equation are given as follows:

$$\nabla \cdot (\vec{v}) = 0 \quad (1)$$

$$\frac{\partial \vec{v}}{\partial t} + (\vec{v} \cdot \nabla) \vec{v} = -\frac{1}{\rho} \nabla P + \mu \nabla^2 \vec{v} - F_d \vec{v} + \vec{G} \quad (2)$$

$$\frac{\partial h}{\partial t} + (\vec{v} \cdot \nabla) h = q + \frac{1}{\rho} \nabla \cdot (k \nabla T) \quad (3)$$

where \vec{v} (m/s) is the velocity vector, q the laser heat source, t (s) the time, P (Pa) pressure, ρ (kg/m³) density, μ (m²/s) viscosity, h (J/kg) the enthalpy, and k (W/(m²·K)) the thermal conductivity. F_d (1/s) is the drag force coefficient and \vec{G} (m/s²) the body acceleration due to body force.

The primary physics models utilized in the simulation encompass laser models and surface forces. For the laser model, a Gaussian heat source is employed to describe the laser energy absorbed by the upper surface and keyhole, as expressed in Equation (4):

$$q = \frac{3P \cdot LA}{\pi \cdot r_0^2} e^{\left(\frac{-3(x^2+y^2)}{r_0^2}\right)} \quad (4)$$

where q (J/(m²·s)) is the laser heat flux absorbed at the free surface at the point (x,y) and LA is the laser absorptance of the material. The heat source is regarded as part of the surface heat flux boundary condition, and the main energy transfer modes in the upper free surface include convection, radiation, and evaporation, which can be expressed as:

$$k \frac{\partial T}{\partial \vec{n}} = q - q_{conv} - q_{rad} - q_{evap} \quad (5)$$

$$q_{conv} = h_c (T - T_{ref}) \quad (6)$$

$$q_{rad} = \sigma \varepsilon (T^4 - T_{ref}^4) \quad (7)$$

$$q_{evap} = \phi L_v P_{atm} \sqrt{\frac{1}{2\pi RT}} \exp\left[\frac{L_v(T-T_b)}{TRT_b}\right] \quad (8)$$

Where \vec{n} is the surface normal vector and h_c (W · m⁻² · K⁻¹) is the heat transfer coefficient. σ (W · m⁻² · K⁻⁴) is the Stefan-Boltzmann constant and ε is the radiation emissivity. For other surfaces, only convection and radiation are considered.

Two significant forces act upon the surface of the liquid metal, causing deformation of the free surface. As the heat source is applied, the temperature of the substrate increases, initiating the melting process. Upon reaching the melting point, surface tension predominantly governs the flow behavior. The surface tension coefficient is estimated as a linear function of temperature to account for the Marangoni effect, expressed in the following equation:

$$\sigma(T) = \sigma_0 - \sigma_s^T (T - T_l) \quad (9)$$

where σ_0 (N · m⁻¹) and σ_s^T are surface tension coefficient at the reference temperature T_l (liquidus temperature) and its temperature sensitivity, respectively. When laser energy irradiates the material, it leads to violent evaporation and the generation of a significant amount of vapor, resulting in recoil pressure. The recoil pressure model employed in this study is described by Equation 10:

$$P_r = \frac{1+\beta_R}{2} * P_{atm} e^{\left(\frac{\Delta H}{R} * \left(\frac{1}{T_v} - \frac{1}{T}\right)\right)} \quad (10)$$

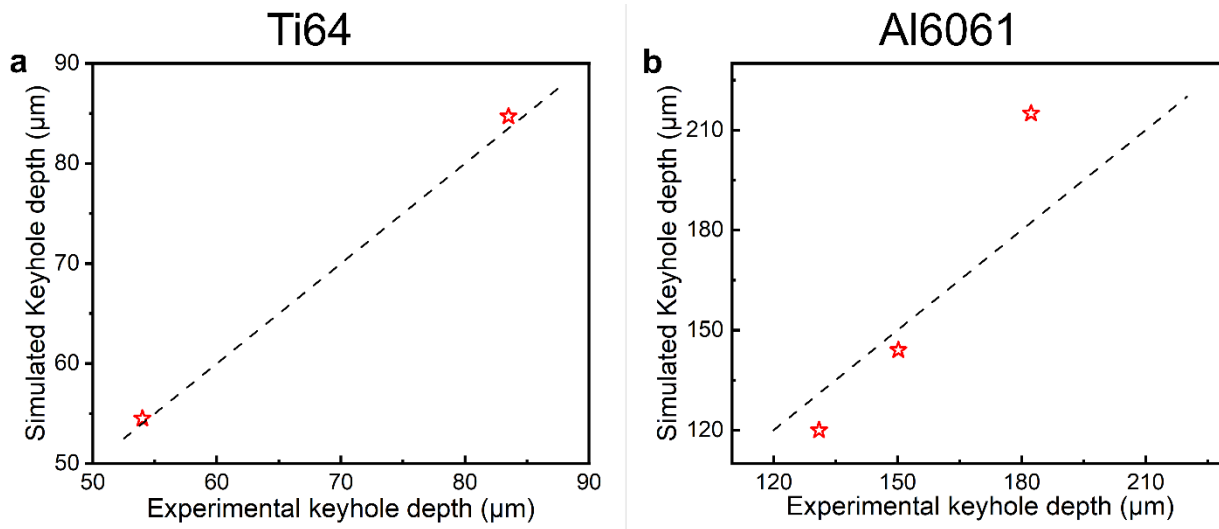
where P_r (Pa) is recoil pressure, β_R is the ratio of recondensation particles to the evaporation ones, P_{atm} (Pa) is the ambient pressure, ΔH (J/mol) is the specific enthalpy of metal vapor, R (J · kg⁻¹ · K⁻¹) is the universal gas constant, T_v (K) is the boiling temperature, and T (K) is the surface temperature. Both surface tension, recoil pressure, and the Marangoni effect are treated as boundary conditions.

The evolution of gas-liquid free surface is tracked by the VOF method:

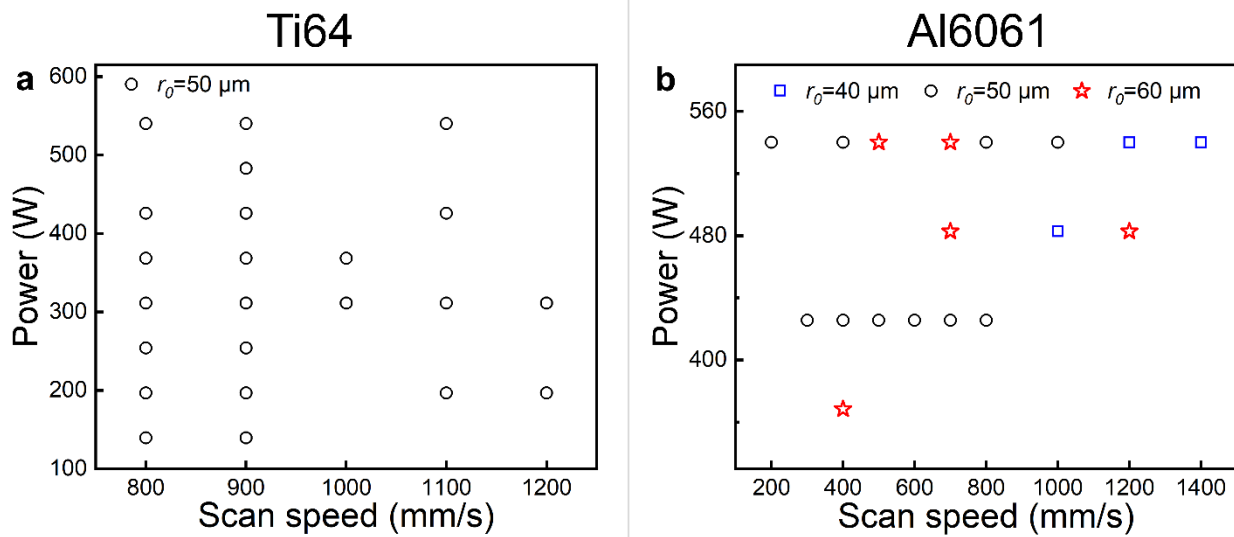
$$\frac{\partial F}{\partial t} + \nabla \cdot (F\vec{v}) = 0 \quad (11)$$

where F is the volume fraction.

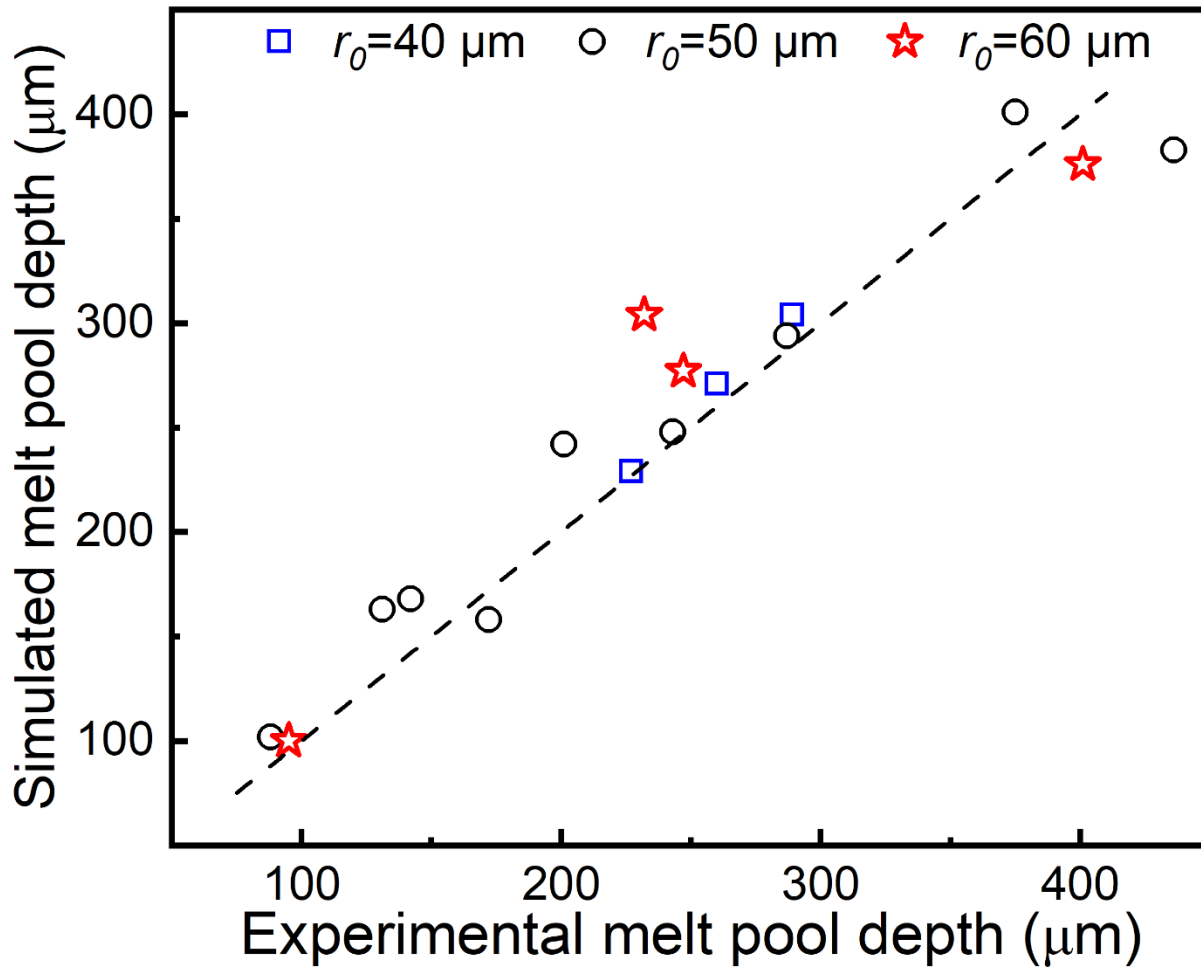
The computational domain for the bare substrate in this study spans dimensions of $1800 \mu\text{m} \times 300 \mu\text{m} \times (H + 150) \mu\text{m}$ (Supplementary Fig. 5). The depth of this computational domain (H) is determined based on various input energy density values, ranging from $300 \mu\text{m}$ to $800 \mu\text{m}$. To maintain both simulation accuracy and computational efficiency, the mesh size is set to $6 \mu\text{m}$ after the mesh-sensitivity analysis. For a comprehensive overview of the thermal properties, which encompass density, thermal conductivity, viscosity, and surface tension, as well as other material properties specific to Ti64 and Al6061 (Supplementary Fig. 6 and Table 1).



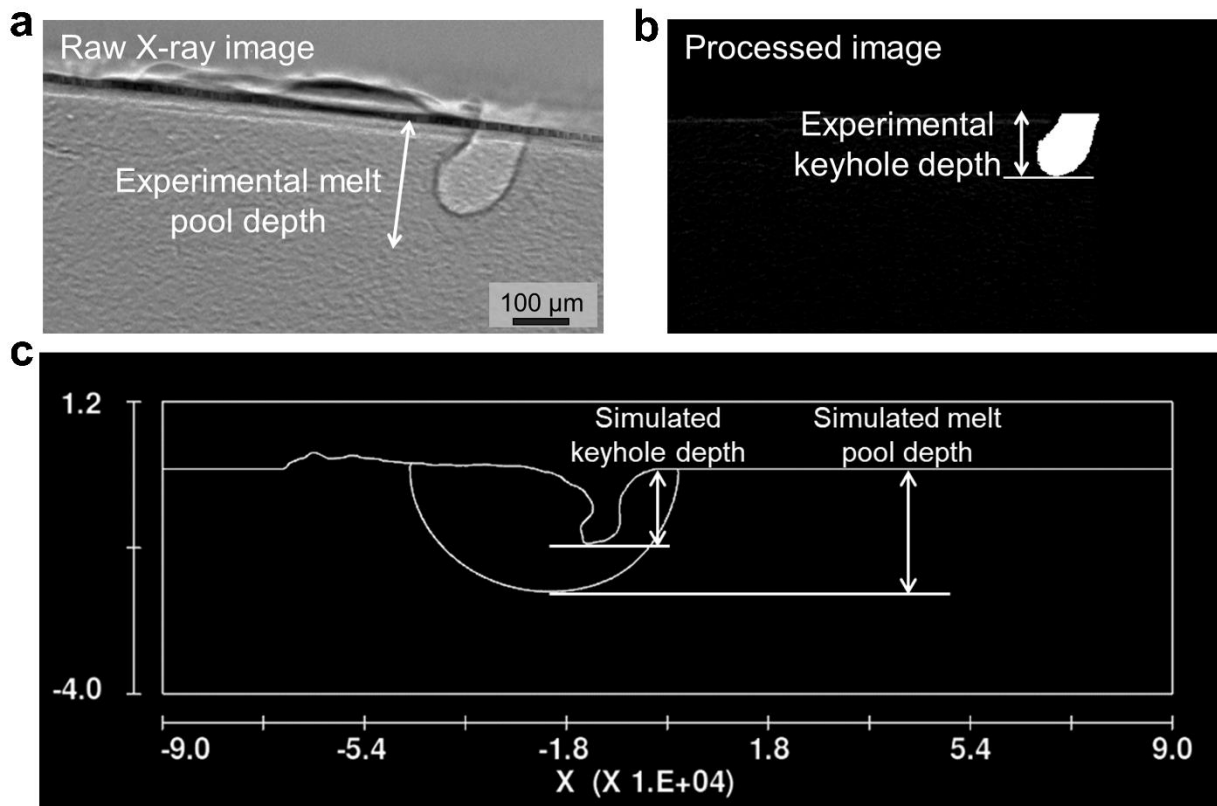
Supplementary Fig. 1. A comparison between the experimental keyhole depth derived from X-ray images and the simulated keyhole depth calculated using experimental laser absorptance (LA).



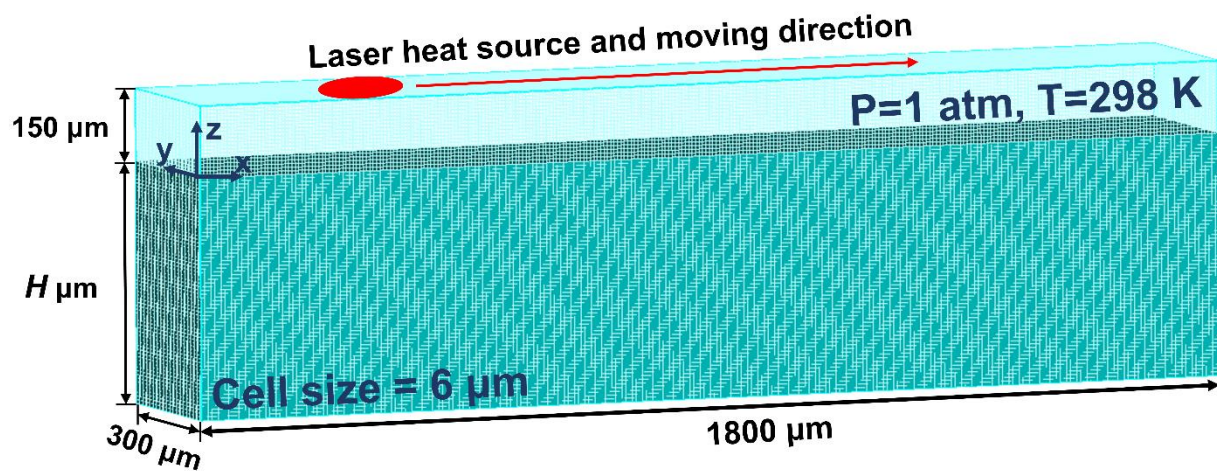
Supplementary Fig. 2. The dataset comprising experimental data for laser absorptance and X-ray images, obtained across a wide range of power (P), velocity (v), and laser spot radius on the sample surface (r_0) combinations. Data points marked with red stars encompass both laser absorptance and their corresponding X-ray images, while data points in different colors exclusively contain X-ray images. **a** Data points for Ti64. **b** Data points for Al6061.



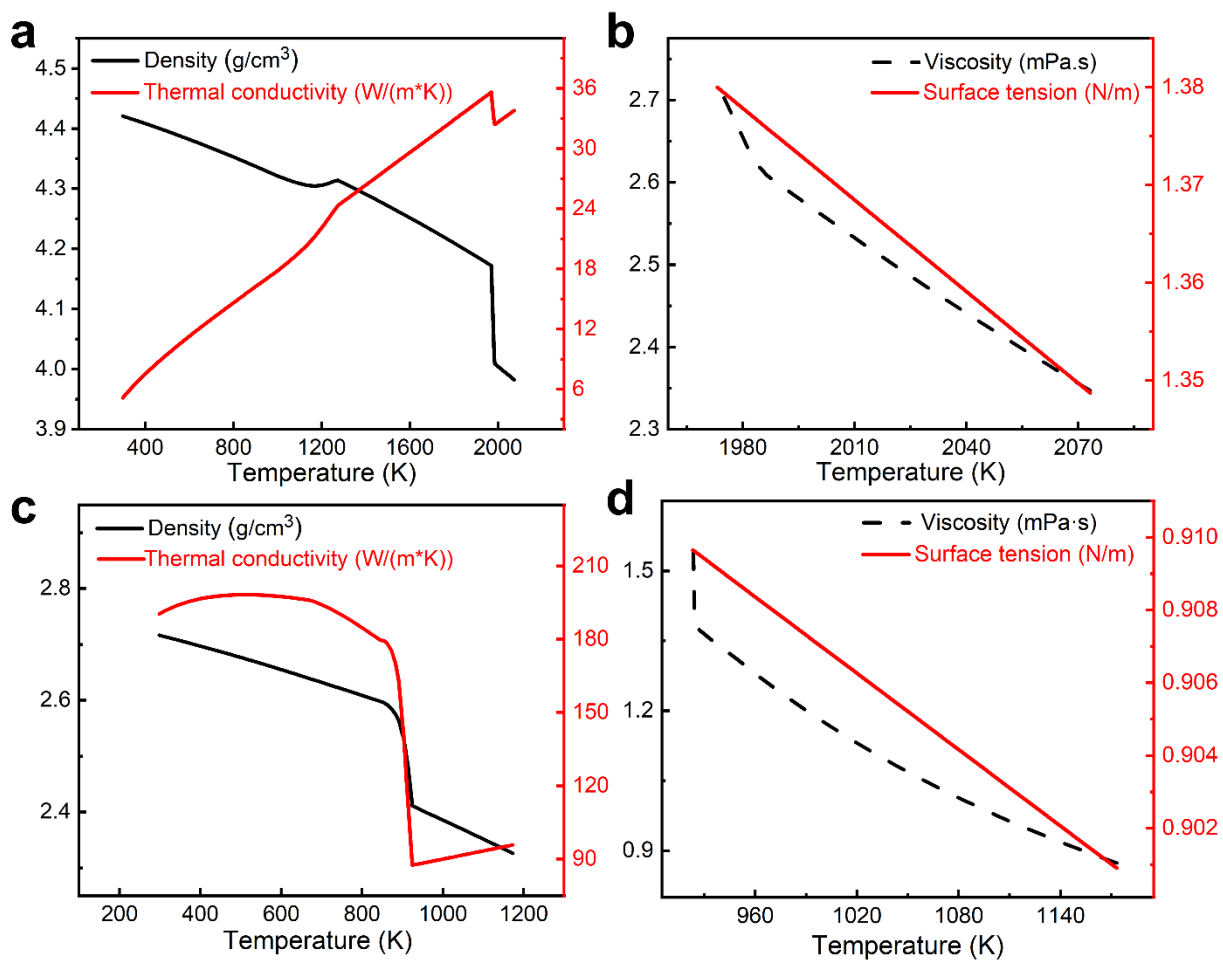
Supplementary Fig. 3. Comparison between experimental melt pool depth and simulated melt pool depth under different surface energy densities for Al6061. The experimental melt pool depths are manually measured from X-ray images for Al6061 due to its distinct contrast.



Supplementary Fig. 4. Supplementary Fig. 4. Representative **a** raw X-ray image, **b** segmented mask, and **c** simulated keyhole morphology at the longitudinal cross section. The experimental X-ray images are segmented to isolate the keyhole area and automatically measure the experimental keyhole depth by the method proposed in Ref³⁸. The simulated keyhole depth and melt pool depth are evaluated by referencing the isotherms corresponding to the saturation temperature and solidus temperature of the material, respectively, as suggested by Gan *et al.*³⁶.



Supplementary Fig. 5. The computational domain for the simulation models, spanning dimensions of $1800\ \mu\text{m} \times 300\ \mu\text{m} \times (H + 150)\ \mu\text{m}$. The depth of this computational domain (H) is determined based on various input energy density values, ranging from $300\ \mu\text{m}$ to $800\ \mu\text{m}$. After the mesh-sensitivity analysis, the mesh size is set to $6\ \mu\text{m}$ to maintain both simulation accuracy and computational efficiency.



Supplementary Fig. 6. The thermal properties encompassing density, thermal conductivity, viscosity, and surface tension for **a, b** Ti64 and **c, d** Al6061.

Supplementary Table 1. Thermal and mechanical parameters for the simulations of Ti64 and Al6061^{21, 31, 47}.

Property	Ti6Al4V	Al6061
Solidus temperature [K]	1878	873.15
Liquidus temperature [K]	1928	915.15
Boiling temperature [K]	3315	2750
Gas constant ($J \cdot kg^{-1} \cdot K^{-1}$)	173.2	308
Latent heat of melting [$J \cdot kg^{-1}$]	2.86×10^5	3.97×10^5
Latent heat of evaporation [$J \cdot kg^{-1}$]	9.7×10^6	1.077×10^7
Saturated vapor pressure [Pa]	1.013×10^5	1.013×10^5
Stefan-Boltzman constant [$W \cdot m^{-2} \cdot K^{-1}$]	5.6704×10^{-8}	5.6704×10^{-8}
Recondensation coefficient β_R	0.08	0.5795
Darcy drag force coefficient	5.57×10^6	3×10^6
Surface tension (N/m)	1.38	0.91
Thermocapillary coefficient (N/(m·K))	3.13×10^{-4}	3.5×10^{-4}

Supplementary Video 1.

The left part of the video demonstrates a real-time laser absorptance measurement and X-ray images captured in Ti64 bare plate under moving laser illumination. The imaging frame rate is 50000 fps. The laser spot radius on the sample surface is 60 μm , the power is 196 W, and the scan speed is 0.7 m/s. The pixel resolution of 1.93 μm . The exposure time for each image is 2.5 μs . The right part of the video shows the isotherms corresponding to the solidus temperature and temperature contour at the longitudinal cross-section from simulation results. The time step for the simulation process is approximately 1 μs .

Supplementary Video 2.

The left part of the video demonstrates a real-time laser absorptance measurement and X-ray images captured in Ti64 bare plate under moving laser illumination. The imaging frame rate is 50000 fps. The laser spot radius on the sample surface is 60 μm in radius, the power is 254 W, and the scan speed is 0.7 m/s. The pixel resolution of 1.93 μm . The exposure time for each image is 2.5 μs . The right part of the video shows the isotherms corresponding to the solidus temperature and temperature contour at the longitudinal cross-section from simulation results. The time step for the simulation process is approximately 1 μs .

Supplementary Video 3.

The left part of the video demonstrates a real-time laser absorptance measurement and X-ray images captured in the Al6061 bare plate under moving laser illumination. The imaging frame rate is 50000 fps. The laser spot radius on the sample surface is 60 μm , the power is 473 W, and the scan speed is 0.7 m/s. The pixel resolution of 1.93 μm . The exposure time for each image is 2.5 μs . The right part of the video shows the isotherms corresponding to the solidus temperature and temperature contour at the longitudinal cross-section from simulation results. The time step for the simulation process is approximately 1 μs .

Supplementary Video 4.

The left part of the video demonstrates a real-time laser absorptance measurement and X-ray images captured in the Al6061 bare plate under moving laser illumination. The imaging frame rate is 50000 fps. The laser spot radius on the sample surface is 60 μm in radius, the power is 500 W, and the scan speed is 0.7 m/s. The pixel resolution of 1.93 μm . The exposure time for each image is 2.5 μs . The right part of the video shows the isotherms corresponding to the solidus temperature and temperature contour at the longitudinal cross-section from simulation results. The time step for the simulation process is approximately 1 μs .

Supplementary Video 5.

The left part of the video demonstrates a real-time laser absorptance measurement and X-ray images captured in the Al6061 bare plate under moving laser illumination. The imaging frame rate is 50000 fps. The laser spot radius on the sample surface is 60 μm , the power is 554 W, and the scan speed is 0.7 m/s. The pixel resolution of 1.93 μm . The exposure time for each image is 2.5 μs . The right part of the video shows the isotherms corresponding to the solidus temperature and temperature contour at the longitudinal cross-section from simulation results. The time step for the simulation process is approximately 1 μs .

Supplementary Video 6.

The comparison between real-time keyhole depth prediction from three different approaches (literature-based simulation, physics-based approach, and machine learning-based approach) and ground truth from experimental X-ray images for Ti64. The laser spot radius on the sample surface is 50 μm , the power is 196 W, and the scan speed is 1 m/s.

Supplementary Video 7.

The comparison between real-time keyhole depth prediction from three different approaches (literature-based simulation, physics-based approach, and machine learning-based approach) and ground truth from experimental X-ray images for Al6061. The laser spot radius on the sample surface is 50 μm , the power is 540 W, and the scan speed is 0.6 m/s.

Supplementary Data 1.

The derived laser absorptance values from the X-ray images acquired from 23 P - v - r_0 combinations for Ti64 and 18 P - v - r_0 combinations for Al6061 in the literature ^{6, 10}.